Supporting Information for:

Imaging of Metal Ion Dissolution and Electrodeposition by Anodic Stripping Voltammetry – Scanning Electrochemical Microscopy

Mario A. Alpuche-Aviles[†,‡], John E. Baur[§], and David O. Wipf*[,†]

Department of Chemistry, Mississippi State University, Mississippi State, MS 39762

Department of Chemistry, Illinois State University, Normal, IL 61790–4160

*Corresponding author. Fax: (662) 325–1618. E-mail: wipf@ra.msstate.edu

[†]Department of Chemistry, Mississippi State University

[§]Department of Chemistry, Illinois State University

[‡]Present Address: Department of Chemistry, The Ohio State University, Columbus, OH 43210

Abstract

Experimental results (Figures S-1 – S-3) illustrate the reproducibility of our signals and some of the problems with the signal to noise discrimination. Also, the synchronization of the tip movement and acquisition of the voltage and current data is shown in Figure S-3. Details of data acquisition and power synchronization are given in page S-5

An example of the determination of Pb dissolved from a Pt substrate by the ASV-SECM method is shown in Figure S-4. This figure presents the original experimental results (Fig. S-4A) obtained from Figure 7 in the paper. Figure S-4A shows the difference between a voltammogram obtained with the tip on top of a Pt substrate electrode and a voltammogram with the tip far away of the Pt electrode. Subtraction of the voltammograms yields the *additional* Pb detected by the tip on top of the Pt electrode. This material is detected since the tip induces Pb dissolution from the Pt surface, and can be quantified from integration of the subtracted voltammogram after

background correction (Fig. S-5B). The Pb equilibrium and electrodeposition discussed in the paper (Table 2) is presented. Figure S-5 shows the equilibrium data for a Pb wire in 0.5 M KNO_3. Calculated rates for the reaction $Pb^{2+} + 2e \rightleftharpoons Pb^0$ are presented in Table S-1.

Details of the numeric simulation are also included here. A mathematical description of the model (page S-7) and details of the final element solver parameters are presented. A list of the dimensionless parameters is given in Table S-2.

Details of tip characterization are given in pages S-12 to S-14

Figures

Tables

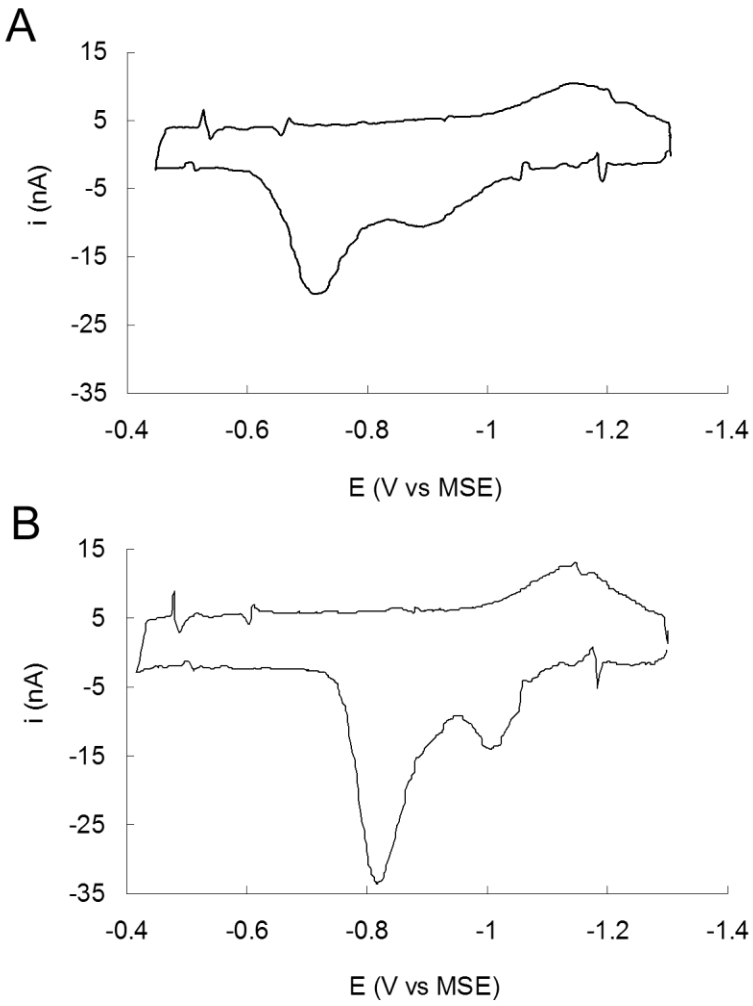

Figure S-1. Fast-scan ASV results in quiescent solutions at a 10 μm diam Hg-Pt film electrode. (A) and (B) are voltammograms for two different electrodes in 5 μM Cd^{2+} and Pb^{2+}/0.5 M KNO_3. The preconcentration potential was –1.3 V vs. MSE, t_p = 300 ms, and v = 100 V/s.

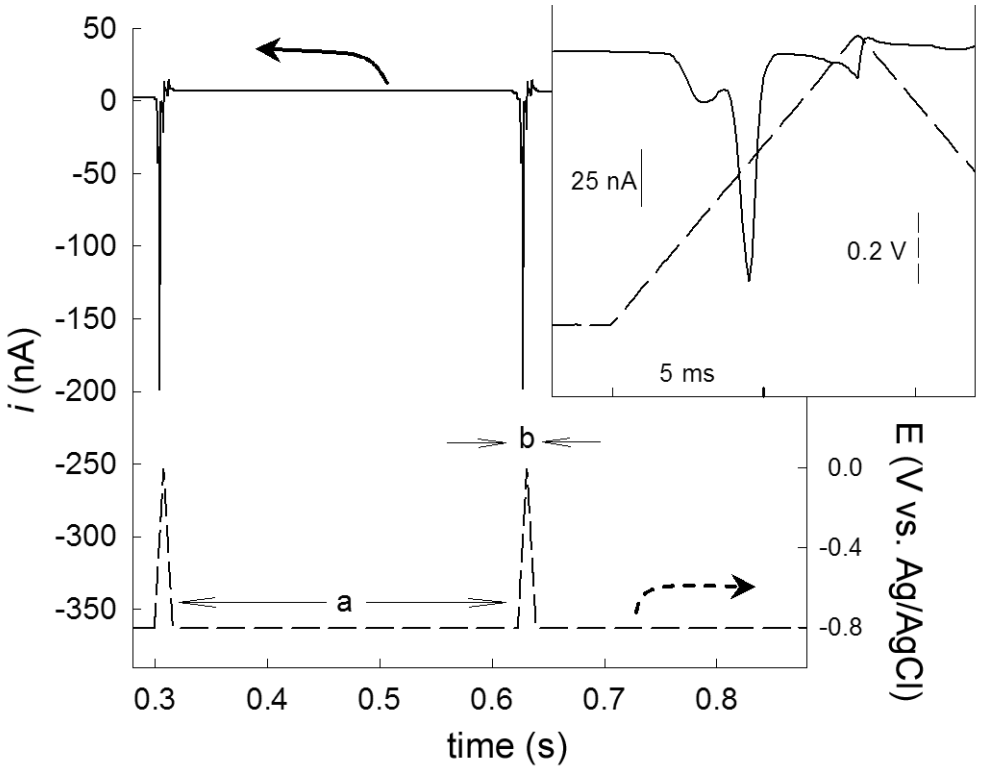

Figure S-2. An illustration showing the synchronized movement of the tip and ASV data acquisition. The tip is moved to a new image point and preconcentration occurs during period *a*. At *b* the tip is stopped to record the stripping voltammogram. (—) Current (- - -) potential. The inset shows an expanded portion of the stripping voltammogram from time *b*.

Data Acquisition and Power Synchronization

An issue found with our ASV data was a large amount 60 Hz power line noise. Voltage scans at 100 V/s produce data in the same frequency range as the 60 cycle power line frequency, making filtering this noise ineffective. We found that using data acquisition synchronized to the power line phase was necessary to avoid large scan-to-scan changes in the background current. With synchronization, all CV scans have essentially the same baseline, simplifying background subtraction (see Figure S-2 for the effect of noise on the data). Although not implemented here, use of higher ASV scan rates will move the data frequency away from the power-line frequency allowing more effective filtering.

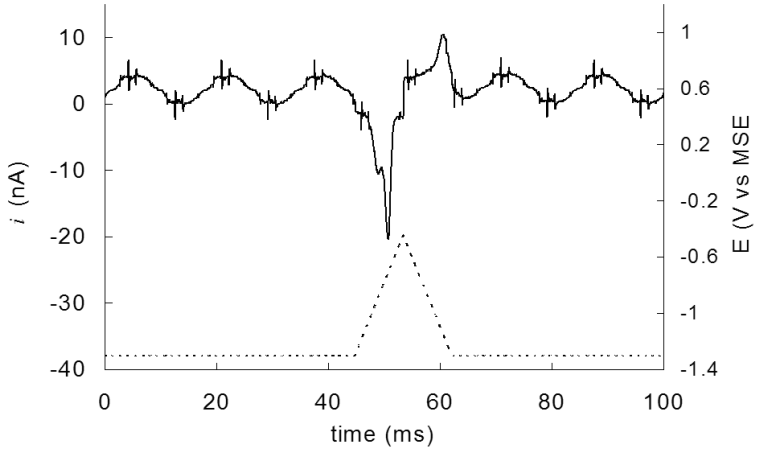

Figure S-3. ASV current (——) and potential (···) traces as a function of time showing the magnitude and reproducibility of the noise produced by the power line.

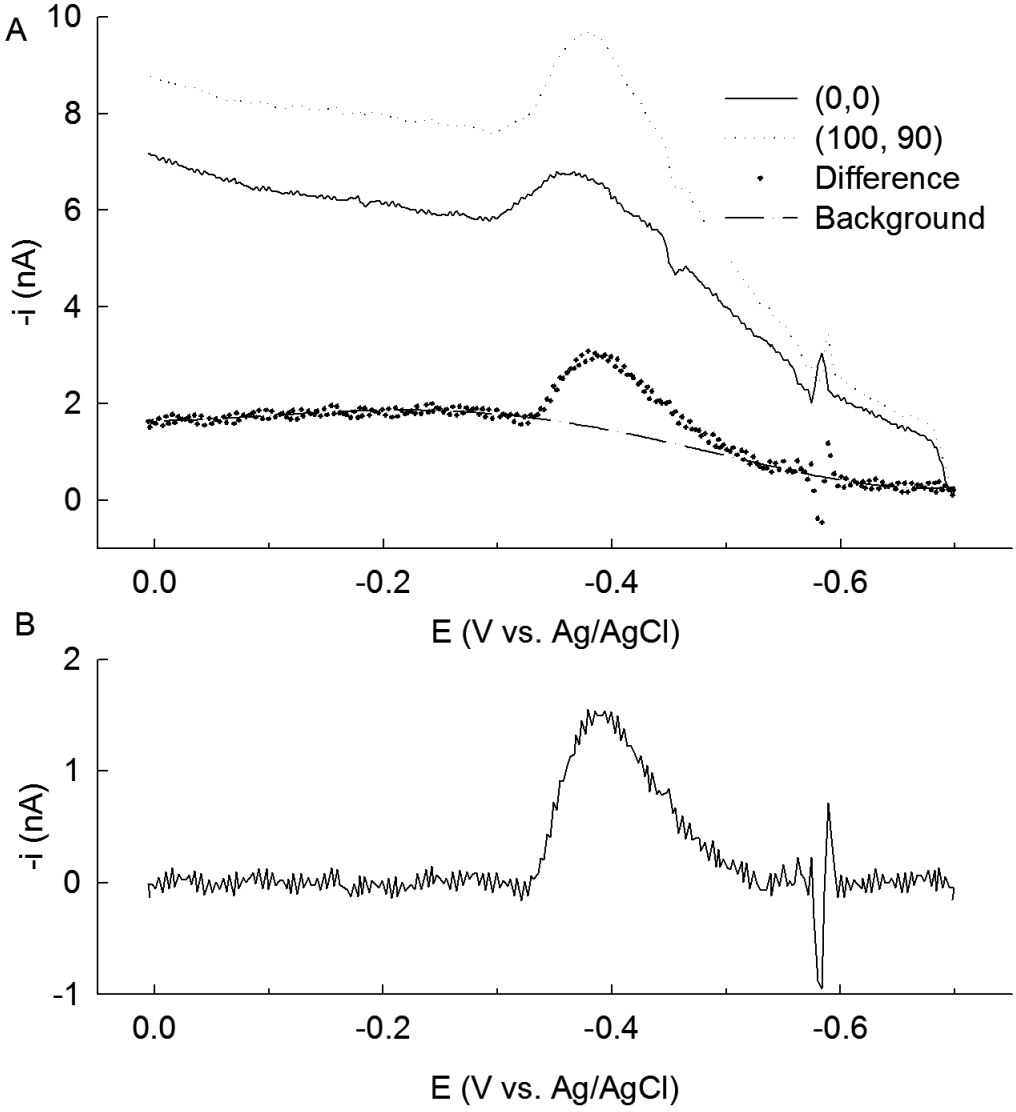

Figure S-4. Graphs illustrating the procedure used to determine the amount of Pb^{2+} induced to dissolve at a Pb coated surface. (A) Individual ASVs (anodic current only) extracted from the ASV-SECM image in Figure 7 at two positions in the image: (—) at (0, 0), which is off the substrate and at the beginning of the image scan and (···) at (100, 90) μm, which is over the Pb-coated substrate at the end of the scan; (•) the difference between the two ASVs and (–·–) an interpolated background. (B) The current difference after background correction. The peak current in B is integrated to provide the stripping charge difference.

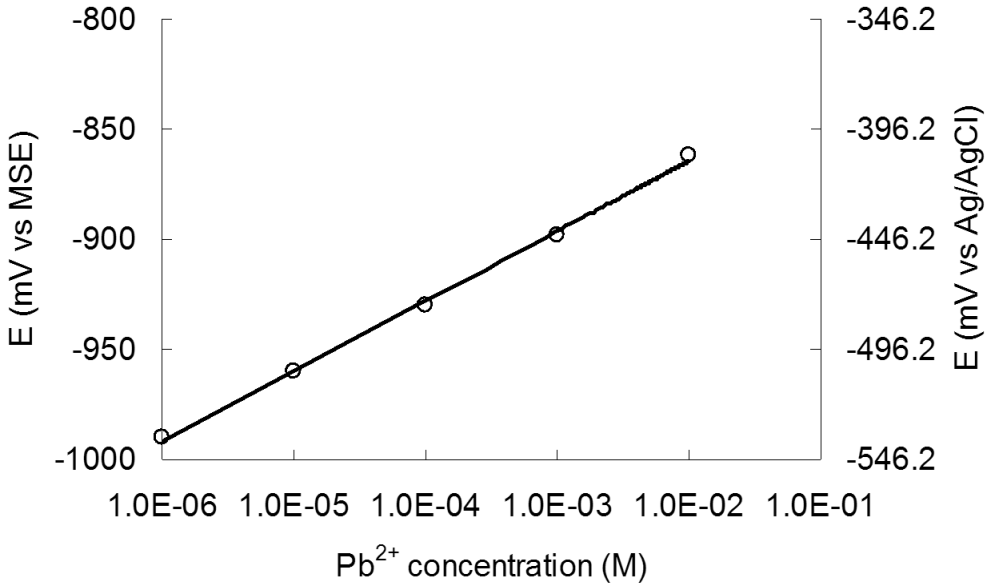

Figure S-5. Experimental equilibrium data for the potential of a Pb wire versus [Pb^{2+}] in 0.5 M KNO_3. (o) experimental data; (——) Regression line of E (mV vs. MSE) as a function of [Pb^{2+}] (M). The regression equation is E = 13.81 ln[Pb^{2+}] – 800.8 with R^2 = 0.9985.

Table S-1. Tabulated kinetic data for $Pb^{2+} + 2e \rightleftharpoons Pb^0$ under experimental conditions used in this work.

[Pb2+] (µM)	**E_{eq} (mV) (vs. Ag/AgCl)**	**$E - E_{eq}$ (mV)**	**current density, j (mA/cm^2)**			**i_a (nA) 10 µm diam**
			j_o	**j_c**	**j_a**	
***E_{sub}* = –600 mV**						
1	–536.2	–63.8	7.05	374	2.62	2.05
100	–476.2	–123.8	17.8	34000	2.58	2.03
***E_{sub}* = –300 mV**						
20	–496.4	–203.6	12.8	4×10^6	0.54	

Simulations

Simulations were carried out with Comsol Multiphysics (version 3.3, Comsol, Burlington, MA) or Comsol Script (version 1.1) in the two-dimensional space shown in Figure S-6. This simulation area had a width (r_{max}) of 100 times and a height (z_{max}) of 50 times the normalized electrode radius ($r_0 = 1$). The reduced variables used for the calculations are shown in Table S-2.

Initial Conditions

$$c_A(r,z,0)=1 \qquad r \notin [0,1] \cup z \notin [0,H] \qquad \text{S1}$$

$$c_B(r,z,0)=0 \qquad r \in [0,1] \cup z \in [0,H] \qquad \text{S2}$$

Boundary Conditions

$$c_A(r_{max},z,t)=1 \qquad \text{S3}$$

$$c_A(r,z_{max},t)=1 \qquad \text{S4}$$

$$\frac{\partial}{\partial z}c_A(r,0,t)=0 \qquad r \in (1,r_{max}] \qquad \text{S5}$$

$$\frac{\partial}{\partial z}c_B(r,0,t)=0 \qquad r \in [0,r_0] \qquad \text{S6}$$

$$\frac{\partial}{\partial r}c_A(0,z,t)=0 \qquad r \in (H,z_{max}] \qquad \text{S7}$$

$$\frac{\partial}{\partial r}c_B(0,z,t)=0 \qquad r \in [0,H] \qquad \text{S8}$$

$$c_A(r,z,t)=0 \qquad r \in [0,r_0] \cup z \in [0,H] \qquad \text{S9}$$

$$c_B(r,z,t)=0 \qquad r \notin [0,r_0] \cup z \notin [0,H] \qquad \text{S10}$$

$$c_A(r,H,t)=c_B(r,H,t)\exp(\tau) \qquad r \in [0,r_0] \qquad \text{S11}$$

$$c_A(r_0,z,t)=c_B(r_0,z,t)\exp(\tau) \qquad z \in [0,H] \qquad \text{S12}$$

$$D_A\frac{\partial}{\partial z}c_A(r,H,t)+D_B\frac{\partial}{\partial z}c_B(r,H,t)=0 \qquad r \in [0,r_0] \qquad \text{S13}$$

$$D_A\frac{\partial}{\partial r}c_A(r_0,z,t)+D_B\frac{\partial}{\partial r}c_B(r_0,z,t)=0 \qquad z \in [0,H] \qquad \text{S14}$$

The grid used for the finite element modeling consisted of approximately 6200 elements. The global predefined grid size was set to "finer," and the maximum element size was set to 0.01 on

the top surface of the Hg film ($z = H$ and $0 \le r \le r_0$) and 0.002 on the edge of the film ($0 \le z \le H$ and $r = r_0$). An element growth rate of 1.08 was used for both of these boundaries. Weak constraints (ideal) were used to improve the accuracy of flux calculations at the boundaries. As a result, fewer elements were needed and thus the calculation time was greatly reduced.

The problem was modeled with the transient diffusion application mode (2d axial symmetry) and solved with the direct (UMFPACK) solver. Two application modes (both transient diffusion) were used, one to model the metal in the Hg film and the other to model the metal ion in the analyte solution. This allowed solution parameters (concentrations, diffusion coefficients, boundaries, etc.) to be set independently for the film and for the solution. The resulting two subdomains interacted only at the Hg-solution interface via the nernstian boundary conditions (Equations S11 and S12) and the flux boundary conditions (Equations S13 and S14), as the metal ion was not active in the Hg film subdomain and the metal was not active in the solution subdomain.

To facilitate comparisons between experimental data and theory, dimensionless starting and switching potentials were calculated from the experimental potential limits (−1.300 to −0.415 V vs. MSE) and the experimental $E_{1/2}$ (−0.775 V vs. MSE). The resulting dimensionless initial potential, τ_i, was −40.9 and the dimensionless switching potential, τ_λ, was +28.0. The simulations were carried out in dimensionless time (T_{sim}); intervals were chosen for the deposition and the voltammogram corresponding to the experimental parameters (t_{dep} = 0 to 300 ms, v = 100 V s^{-1}). During deposition, the interval between points was equivalent to one point per ms except for the 4 ms deposition time, which had 10 points per ms. Each voltammogram consisted of 3000 points, equivalent to a potential spacing of about 0.55 mV (n = 2).

The three-dimensional normalized current, $\psi(T_{sim})$, was calculated by integrating the time-dependent flux over the Hg-solution boundary (using the integration coupling variable feature of the software) and multiplying by $\frac{2\pi r_0}{4}$. It should be noted that since weak constraints were used, in practice the Laplace multiplier (variable lm1 in the simulation) was actually integrated over the Hg-solution boundary. Since the flux is equal to −lm1/r, $\psi(T_{sim})$ was calculated by integrating lm1 over the boundary and multiplying the result by $-\frac{2\pi}{4} = -\frac{\pi}{2}$.

For simulations of multiple ASV cycles, the final calculated solution for one voltammogram was used as the initial value for the next cycle of the solver. All the dimensionless current-potential pairs for each cycle were stored for later analysis.

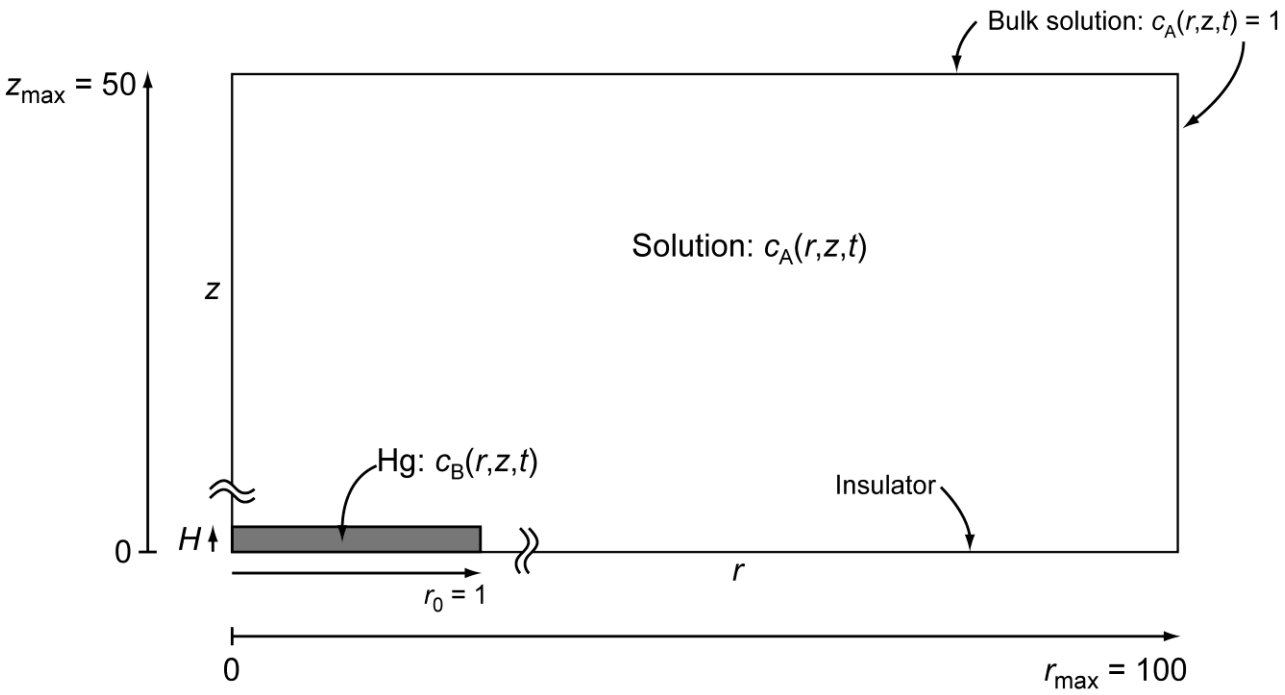

Figure S-6 Simulation space used for calculations.

Table S-2. Variables and normalized variables used for simulations.

Variable and Relationship	Value	Description
a	5.0×10^{-4} cm	Electrode radius (cm)
C_s^*	0.10×10^{-6} mol cm^{-3}	Bulk concentration of metal ion in solution (mol cm^{-3})
D_s	8.16×10^{-6} mol cm^{-2}	Diffusion coefficient of metal ion in solution (cm^2 s^{-1})
D_{Hg}	14.1×10^{-6} mol cm^{-2}	Diffusion coefficient of metal in Hg (cm^2 s^{-1})
l	4.4×10^{-6} cm	Hg film thickness (cm)
v	100 V s^{-1}	Scan rate (V s^{-1})
$c_A(r,z,t) = \frac{C_s(r,z,t)}{C_s^*}$		Dimensionless metal ion concentration in solution
$c_B(r,z,t) = \frac{C_{Hg}(r,z,t)}{C_s^*}$		Dimensionless metal concentration in Hg
$D_A = \frac{D_s}{D_s} = 1$	1	Dimensionless diffusion coefficient of metal ion in solution
$D_B = \frac{D_{Hg}}{D_s}$	1.73	Dimensionless diffusion coefficient of metal in Hg
$H = \frac{l}{a}$	0.0088	Dimensionless film thickness
$r_0 = a/a = 1$	1	Dimensionless radius
V or $p^2 = \frac{a^2 nFv}{D_s RT}$	238.6	Dimensionless scan rate
$T_{sim} = \frac{D_s t}{a^2}$		Dimensionless time
$\tau = \frac{nF(E - E_{1/2})}{RT}$		Dimensionless potential
$\psi = \frac{i}{4nFaDC_s^*}$		Dimensionless current

TIP CHARACTERIZATION

Hg Film Electrodes

Attempts to make Hg thin film electrodes by amperometry did not yield smooth coatings and tended to produce small drops on the edge of the Pt surface. This is as expected from the previously reported mechanism of Hg nucleation and diffusion-limited growth on a Pt surface.[1] Subsequent experiments using CV deposition found that scan rates of 50-100 V/s produced more uniform Hg films. Deposition CVs start at a potential just negative of the half wave potential of the Hg voltammogram on Pt. Wider potential ranges (into H_2 evolution) and higher scan rates were found to produce smoother films (i.e. method 1), as observed with the optical microscope. Slower scan rates (20-50 V/s) and a smaller potential window yielded a rougher deposit of Hg, presumably due to a higher amount of Hg being deposited on the Pt surface (method 2). Method 1 electrodes were used for ASV experiments, since they provided better peak separation at 100 V/s than method 2 electrodes, which had broader Pb^{2+} ASV peaks.

The amount of Hg deposited at the tip for method 1 electrodes was $(2.32 \pm 0.5) \times 10^{-13}$ moles ($n = 4$) as estimated from the Hg oxidation peak. The oxidation peak was 0.6 V positive of the standard Hg oxidation potential, indicating that Hg has formed an amalgam with the Pt substrate.[2, 3] The solubility of Pt in Hg is not well established—reports range from 5×10^{-4} to 0.1 atomic % (5×10^{-4} at % is the recommended value at room temp).[4] Thus, given the uncertainty in film composition and stoichiometry, the film thickness could not be calculated. However, were the film composed of pure Hg, the estimated thickness would be (44 ± 9) nm.

Cd and Pb Stripping Peaks in Quiescent Solution

The charge ratio of Pb/Cd of ~1.19 cannot be accounted for by dissolution kinetics and is due to the different Pb^{2+} and Cd^{2+} diffusion coefficients (see Table 2). During the preconcentration step, the reduction of these ions is at the mass transport limit. The preconcentration charge passed can be estimated by numerical integration of an analytical expression for the current at an embedded microdisk electrode.[5] The resulting Pb^{2+}/Cd^{2+} preconcentration charge ratio is 1.17, in reasonable agreement with the stripping charge. This strongly suggests that the different peak height/concentration ratio for Pb^{2+} and Cd^{2+} ions is the

combined result of the difference in the amounts of preconcentrated metal due to differences in diffusion coefficient and dissolution rate from the Hg/Pt amalgam.

The ratio between the amounts of charge (i.e. reduced material) found in the stripping peak and the expected charge from the steady-state preconcentration current is ~2.0 rather than the expected value of unity. An explanation for the increased ratio is based on the use of continuous sweeping. During the 300 ms preconcentration step, the electrode reduces metal ions from solution. The metal ions are released to solution by stripping over a period of 6-10 ms. Because the tip potential is swept back to the preconcentration potential; the ions are immediately re-reduced during the subsequent 300 ms preconcentration period. In addition, new ions from the bulk are reduced during the preconcentration step. This produces a stripping peak that increases for several cycles. Eventually, the peak will stop increasing as the rate of loss of stripped ions matches the gain from bulk solution.

We simulated the preconcentration-stripping cycles on a Hg film UME to support this hypothesis. Simulation results for Pb at a 44 nm thick Hg film are shown in Figure 4 for different preconcentration times, t_p. Both the cathodic and anodic (stripping) currents increase initially until they reach a constant value (Figure 4A and B), with the anodic current being higher than the cathodic due to the effects of t_p. The ASV current becomes constant after around 10 cycles, and for the values of t_p in Figure 4, these 10 cycles would correspond to < 4 s of experimental time. Normalizing the final ASV peak by the first ASV peak gives a ratio of 1.6-1.9, which depends on t_p (Figure 4C). It is worth noting that this ratio does not increase monotonically with t_p, probably due to the complex relationship between linear and convergent diffusion at shorter and longer times.

Additional proof of the validity of the simulations comes from comparing the results for t_p = 300 ms with the experimental results in Figure 3 summarized in Table 1. The final stripping peak values from the simulations at the 60th cycle is for Pb, i_p = 509 nA Q_p = 219 pC, and for a similar simulation for Cd: i_p = 406 nA Q_p = 174 pC (not shown). The simulated peak current shapes appear very different from the experimental ones, due to the Nernstian behavior assumed for the simulation (see supporting information). More accurate simulations of the shape of the experimental stripping peaks would require including kinetic parameters for the stripping process, which is beyond the scope of this paper. However, the stripping charge is independent of these kinetic limitations and the simulated charges agree with our experimental result with an

error of 9 % for Pb and 14 % for Cd. This error is satisfactory since it includes the delay on the power-line synchronization, error in the film thickness measurement and also any possible simulation error.

References

(1) Scharifker, B.; Hills, G. *J. Electroanal. Chem.* **1981**, *130*, 81-97.
(2) Baldo, M. A.; Daniele, S.; Mazzocchin, G. A. *Electrochim. Acta* **1996**, *41*, 811-818.
(3) Kolpakova, N. A.; Borisova, N. V.; Nevostruev, V. A. *J. Anal. Chem.* **2001**, *56*, 744-747.
(4) Guminski, C.; Galus, Z. In *Metals in Mercury*; Hirayama, C., Galus, Z., Guminski, C., Eds.; Pergamon Press: Oxford, **1986**; Vol. 25, pp 330-334.
(5) Szabo, A.; Zwanzig, R. *J. Electroanal. Chem.* **1991**, *314*, 307-311.